CrossMark

On the robustness of near term climate predictability regarding initial state uncertainties

Agathe Germe[1] · Florian Sévellec[2] · Juliette Mignot[1,3] · Didier Swingedouw[4] ·
Sebastien Nguyen[1]

Abstract A set of four ensemble simulations has been designed to assess the relative importance of atmospheric, oceanic, and deep ocean initial state uncertainties, as represented by spatial white noise perturbations, on seasonal to decadal prediction skills in a perfect model framework. It is found that a perturbation mimicking random oceanic uncertainties have the same impact as an atmospheric-only perturbation on the future evolution of the ensemble after the first 3 months, even if they are initially only located in the deep ocean. This is due to the fast (1 month) perturbation of the atmospheric component regardless of the initial ensemble generation strategy. The divergence of the ensemble upper-ocean characteristics is then mainly induced by ocean–atmosphere interactions. While the seasonally varying mixed layer depth allows the penetration of the different signals in the thermocline in the mid-high latitudes, the rapid adjustment of the thermocline to wind anomalies followed by Kelvin and Rossby waves adjustment dominates the growth of the ensemble spread in the tropics. These mechanisms result in similar ensemble distribution characteristics for the four ensembles design strategy at the interannual timescale.

1 Introduction

Seasonal to decadal climate prediction is a very active area of research (e.g. Kirtman et al. 2013) born from a strong societal demand. Its physical principle is based on the long inertia of a few components of the climate system, and notably the ocean, which may lead to longer climate predictability than the atmosphere only. Indeed, predictability in the atmosphere circulation is believed to last up to 2 weeks at most (Lorenz 1963, 1969), while climate model experiments show predictability of the ocean circulation up to a decade ahead (e.g. Keenlyside et al. 2008; Msadek et al. 2010; among many others). Given the potentially large impact of ocean circulation on sea surface temperatures—SST (McCarthy et al. 2015) and therefore on regional climate (Goldenberg et al. 2001; Sutton and Hodson 2005; Zhang and Delworth 2006; Sutton and Dong 2012; Peings and Magnusdottir 2014; Buchan et al. 2014), the ocean circulation predictability may lead to climate predictability in specific regions.

The recent progresses of oceanic observations and reanalyses enable the initialization of the ocean component of the climate system, which is of primary importance for relevant predictions. Yet for climate, as for weather prediction, small differences in the initial state may evolve into considerably different states. This sensitivity implies to take a very specific care of the initial condition uncertainties

✉ Agathe Germe
  agathe.germe@locean-ipsl.upmc.fr

1 LOCEAN Laboratory-IPSL, Sorbonne Universités (UPMC, Univ Paris 06)-CNRS-IRD-MNHN, 4 place Jussieu, 75005 Paris, France

2 Ocean and Earth Science, University of Southampton, Southampton, UK

3 Climate and Environmental Physics and Oeschger Centre for Climate Change Research, University of Bern, Bern, Switzerland

4 Environnements et Paléoenvironnements Océaniques et Continentaux (EPOC), UMR CNRS 5805 EPOC - OASU - Université de Bordeaux, Allée Geoffroy Saint-Hilaire, 33615 Pessac, France

in order to perform reliable near-term climate predictions. Nevertheless, the impact of oceanic uncertainties on those predictions has been poorly investigated so far.

Given its relative accessibility, the surface of the ocean has always been the most observed part of the ocean. This has been strongly reinforced since the satellite era. Even so, disparities remain between different datasets of SST (e.g. Kennedy 2014). At intermediate depth, the Argo floats measurements have strongly improved estimates of the ocean mean state and, to a lesser extent, variability, but here again, strong uncertainties remain (e.g. Abraham et al. 2013). Prior to the 2000s, the intermediate depths were sparsely observed. The deep ocean (below the Argo float sampling, i.e. 2000 m) is still sparsely observed today. Because of the supposed weak decadal variability at such depths, it is commonly assumed that this should not affect decadal prediction studies. However, Sévellec and Fedorov (2013) demonstrated the strong sensitivity of the upper ocean temperature to small density disturbances in the deep ocean on decadal timescales. This result thus suggests that the deep ocean uncertainties might in fact be a strong limitation for near-term climate predictions. Ultimately, ocean observations uncertainties lead to strong disparities among the reanalyses commonly used to initialize the ocean component for near-term climate predictions (e.g. Ray et al. 2014; Born et al. 2015; Karspeck et al. 2015), thereby limiting their robustness (Kröger et al. 2012; Bellucci et al. 2013).

In near-term climate predictions, as for seasonal predictions, initial condition uncertainties are acknowledged by performing an ensemble of predictions. In principle, the way the ensemble is generated should reflect the initial state uncertainties. It may impact its future evolution, and therefore the predicted state and its reliability. Several techniques among the wide range of methods explored in seasonal prediction (Stockdale et al. 1998; Stan and Kirtman 2008) have been used so far. Common methods consist in adding random perturbations or perturbation patterns assessed by singular vectors, to the atmospheric state. These methods have also been extensively used for near-term predictions (Griffies and Bryan 1997; Pohlmann et al. 2004; Collins et al. 2006; Swingedouw et al. 2013; Persechino et al. 2013; Hazeleger et al. 2013). Yet, as they do not take into account oceanic uncertainties, these techniques, which are optimized for the short-term, may give only an upper limit of predictability at interannual to decadal timescales. They may thus yield under-dispersed predictions, which might therefore be poorly reliable. In more recent studies, several techniques, such as using lagged atmospheric and oceanic states (Smith et al. 2007; Baehr and Piontek 2014), different oceanic reanalysis datasets (Du et al. 2012; Pohlmann et al. 2013; Müller et al. 2014), fast-growing perturbation

patterns assessed by a breeding technique (Ham et al. 2014; Baehr and Piontek 2014) or anomaly transforms (Romanova and Hense 2015), have been proposed to take into account oceanic uncertainties. Unfortunately, very few analyses focused on the divergence of the ensemble itself to give insight on the impact of using one method or another. As one of the few, Du et al. (2012) investigated the impact of atmospheric-only (daily lagged method), oceanic-only (different reanalysis datasets) and combined ocean–atmosphere initial state perturbations. They showed that for atmospheric variables such as precipitation or 2-m temperature, there is no noticeable impact of the perturbation technique. On the other hand, they found that oceanic perturbations have an impact on the ensemble characteristics of oceanic variables. This is consistent with findings of Stan and Kirtman (2008), who showed that uncertainties in oceanic initial conditions is a dominant limiting factor for ENSO predictability in comparison to the noise due to internal dynamics of the atmosphere. More recently, Baehr and Piontek (2014) found an improved reliability of their ensemble for timescale from 1 month up to 3 years with the implementation of oceanic bred vectors as compared to lagged initialization. Romanova and Hense (2015) found that temperature disturbances might play a major role in the growth of the ensemble spread compared to perturbations in salinity field or zonal and meridional velocity fields. However, the added value of their technic compared to the previously mentioned methods still needs to be investigated.

Here, we investigate the impact of accounting for oceanic initial state uncertainties versus the classical approach accounting for atmospheric state uncertainties on the predictability of the climate system in a perfect model framework. Initial shock or drift, resulting from initialization toward the observations (Sanchez-Gomez et al. 2015) and the existence of inherent model biases, likely impact the ensemble mean and spread and therefore the prediction and its reliability. The perfect model framework enables us to investigate the effects of the initial perturbations (i.e. the uncertainties) without any disturbance from initial shock or drift on the ensemble behaviour. In particular, the impact of the vertical repartition of the oceanic uncertainties—the deeper ocean being much less observed than the upper ocean—is examined. Several ensembles using different perturbation strategies, all based on white noise perturbations of the oceanic temperature and further described in the Sect. 2, are performed. We use random white noise perturbation in the aim of evaluating the impact of perturbations built up without any a priori information on the ocean state, dynamics or uncertainties. This first step constitutes a robust benchmark for future perturbation analyses taking into account further knowledge of the ocean dynamics and oceanic

uncertainties in the real word. In Sect. 3, the following issues are addressed: (1) How do the oceanic and atmospheric initial perturbations spread in the climate system along the forecast range? (2) What is the impact on the predictability assessment? Conclusions are given in the final section.

2 Methods

2.1 Model

We use the IPSL-CM5A-LR climate model (Dufresne et al. 2013), which was used for several decadal prediction studies in a perfect model context (Persechino et al. 2013; Servonnat et al. 2014) as well as in historical conditions (Swingedouw et al. 2013; Séférian et al. 2013; Ray et al. 2014; Mignot et al. 2015). The atmospheric general circulation model LMD5A (Hourdin et al. 2013) has $1.875° \times 3.75°$ horizontal resolution and 39 vertical levels. It is coupled with the oceanic model NEMOv3.2 (Madec 2008) in the ORCA2 configuration corresponding to a nominal resolution of 2°, enhanced over the Arctic and subpolar North Atlantic as well as around the Equator. There are 31 vertical levels for the ocean with the highest resolution in the upper 150 m. It includes the sea ice model LIM2 (Fichefet and Maqueda 1997) and the biogeochemistry model PISCES (Aumont and Bopp 2006). The coupling between oceanic and atmospheric models is achieved using OASIS3 (Valcke 2006). The reader is referred to the special issue of Climate Dynamic (vol 40, issue 9–10) for analysis of various aspect of this climate model. The performance of the oceanic component in the coupled model is also discussed in Mignot et al. (2013).

2.2 Protocol

We consider the 1000-year long pre-industrial control simulation (thereafter CTL), which has been performed with the IPSL-CM5A-LR model. It starts from a former spin-up phase of a few thousands years. Its first year is arbitrary labelled 1800. We consider a portion of 20 years of this simulation, selected because it comprises an extreme AMOC event at year 2071 (Persechino et al. 2013; Ortega et al. 2015). Four 10-member ensembles are generated from the 1st January 2056 of CTL, 15 years before the 2071 AMOC peak. All ensembles are integrated for 20 years and use the same constant external conditions. The ensembles differ by the generation strategies, which have been designed to address the specific questions introduced above (see Table 1 for a summary).

One atmospheric perturbed ensemble (ATM hereafter) is generated by adding an anomaly randomly chosen in the interval ±0.05 K to the SST field passed to the atmosphere during the first coupling time step, which corresponds to the 15P ensemble described in Persechino et al. (2013). A second ensemble (3D) is generated by adding a Gaussian white noise on the three-dimensional oceanic temperature field. This white noise has a standard deviation (STD) of 3.5×10^{-3} K scaled by the relative volume of each grid cell. This procedure ensures a spatially homogeneous variance despite the irregular grid, meaning that the white noise characteristics (i.e. mean and STD) are the same for water parcels of identical volume whatever the discretization of the parcels. Note that consequently, this procedure addresses the question of the impact of oceanic perturbations on an ensemble evolution, but not the one related to the vertical profile of oceanic uncertainties. The latter is addressed in a different way described further down. In the 3D ensemble, anomalies in the North Atlantic are typically within ±0.05 K at the surface, and ±0.008 K at 3000 m depth, where the grid cells are the largest. The 3D10 ensemble is the exact replication of 3D but the initial perturbation of the ocean temperature field has been multiplied by a factor 10. A 3D100 ensemble has also been generated following the same logic. It yields similar results as 3D10, demonstrating saturation of the initial uncertainties impact, and it is thus not shown here. Finally, in the aim of taking into account the sparseness of oceanic observations in the deep ocean as compared to the intermediate and surface ocean and evaluating the impact of this on the prediction, a third oceanic perturbed ensemble (DEEP hereafter) corresponds to the 3D perturbation field restricted below 2000 m depth (i.e. below the standard ARGO floats sampling) with

Table 1 Summary of the characteristics of the four different ensembles

Ensemble name	Initial perturbed field	Number of members	Start date	Length
ATM	Coupler SST	10	1st January 2056	20 years
3D	3D oceanic temperature	–	–	–
3D10	3D oceanic temperature	–	–	–
DEEP	Deep 3D oceanic temperature (below 2000 m)	–	–	–

When referring to any ensemble, the term DEC is used in contrast to CTL

no perturbation above 2000 m depth. Note that the three oceanic perturbed ensembles (3D, 3D10 and DEEP) share the exact same white noise patterns aside the already mentioned differences (scaling in 3D10, masking in DEEP). This ensures that differences among these ensembles do not arise from round off errors in the initial state. Furthermore, in accordance with real oceanic uncertainties, none of these perturbations (3D, 3D10, or DEEP) is density compensated in salinity. When referring to the decadal ensembles in general, the abbreviation DEC will be used.

The zero-centred white noise perturbation technique assumes that the initial state is perfectly known in term of accuracy but with imperfect precision. Thus, no conclusion can be made here on the impact of a bias of the initial state on the prediction from our experiments. Such a pattern of uncertainties can arise from a perfectly homogeneous measurement survey of the oceanic state by instruments having perfect accuracy, but imperfect precision, for instance. Even though such a perfect oceanic state assessment is far from being achieved, it remains an objective of ocean survey. Our analysis gives an insight on oceanic uncertainties impact on climate predictability in this context.

3 Potential predictability

We use the prognostic potential predictability (PPP) as defined by Pohlmann et al. (2004) to investigate the impact of the ensemble strategy on the predictability. This is computed as:

$$\text{PPP(t)} = 1 - \frac{\sigma_{DEC}(t)}{\sigma_{CTL}}, \tag{1}$$

where $\sigma_{DEC}(t)$ is the ensemble STD referring to the ensemble mean, and σ_{CTL} the temporal STD from CTL experiment. Figure 1 show the significant PPP of the SST for 2–5 years forecast range according to a Fisher test (F-test) at the 99 %-confidence level. These PPP values being assessed from one starting date only, we used such a high confident level in order to give robust conclusions on local PPP. The general pattern of the PPP is found to be very similar among the ensembles, highlighting the high PPP in the subpolar North Atlantic Ocean in contrast to the rest of the ocean (Fig. 1). This global pattern is in accordance with findings of Pohlmann et al. (2004) in another climate model. Note that, in this model using the exact same ensemble (ATM), the sensitivity of the PPP
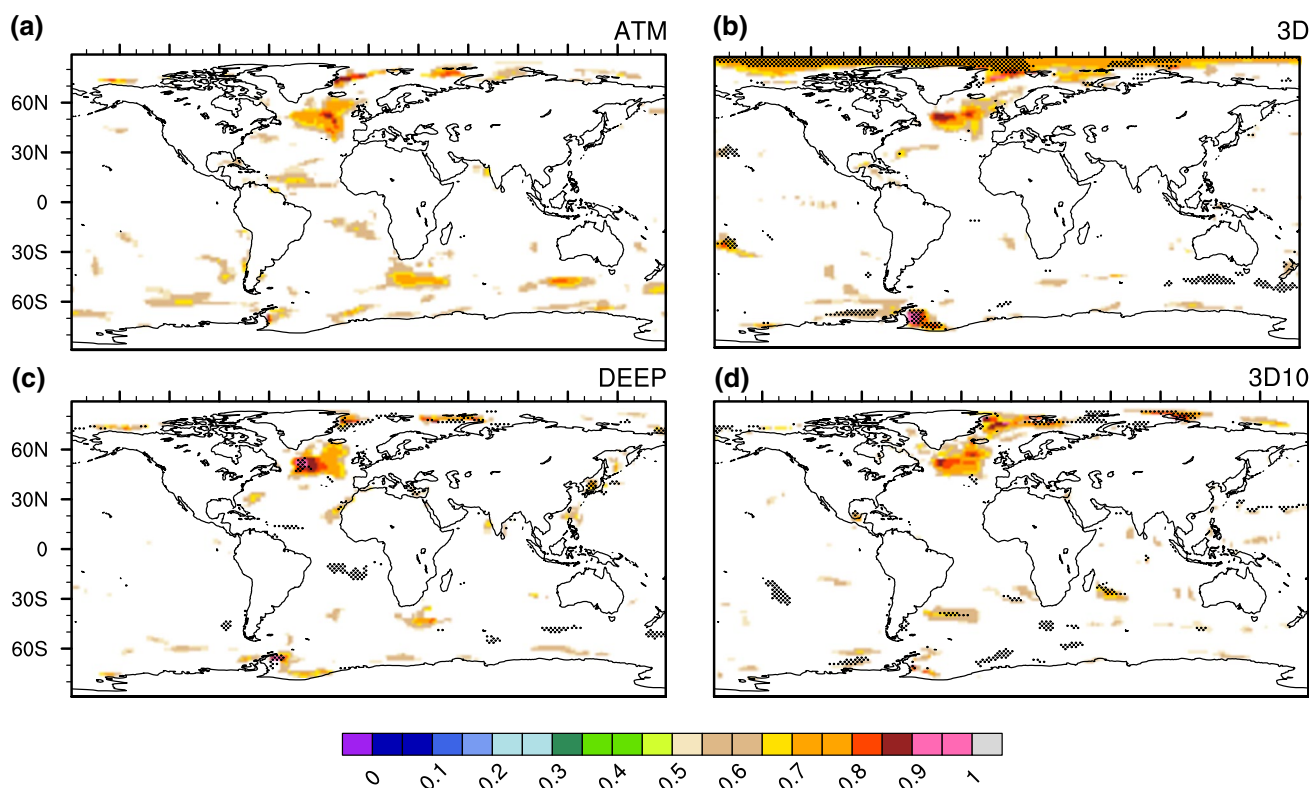

Fig. 1 PPP of SST at 2–5 year forecast range, for **a** ATM, **b** 3D, **c** DEEP and **d** 3D10. *White areas* indicate non-significant PPP according to a F-test at 99-confidence level. In **b**–**d** *black dotted areas* indicate PPP significantly different from the PPP in ATM at the 99-confidence level

to the start date has been shown to be weak in this region by Persechino et al. (2013, specifically their Figure 9b), thereby giving confidence to the robustness of this figure. Other regions appear to be potentially predictable, but these regions differ from one ensemble to the other and the patterns are generally noisy and patchy. Apart from few exceptions, differences with the ATM ensemble are not significant (dark dotted areas in Fig. 1) suggesting that they are not robust. Similar results (not shown) are found for the temperature averaged in the upper 300 m, which has been shown to be more appropriate to look at predictable fluctuations on decadal time scale by Branstator and Teng (2010). The most striking exception regarding the SST is the high PPP obtained in the Arctic Ocean, as well as the Weddell Sea for 3D and not for the other ensembles. These areas are mainly located under perennial sea ice where the SST remains very close to the freezing point with a very weak variability. Therefore, the PPP should be taken very cautiously in these regions. In order to increase the signal-to-noise ratio and thus the reliability of our conclusions, we consider the time evolution of the ensemble mean and spread of the annual SST integrated over the Arctic Ocean (Fig. 2a, b). The four ensembles exhibit similar behaviour with no significant difference for 3D. For the four ensembles, the ensemble spread is not significantly smaller than the CTL STD (Fig. 2b), thus leading to no significant PPP of the SST in this region. In Fig. 1, other significant differences with ATM are found in the Southern Ocean south of Africa in 3D10, or south of Australia in 3D. However, they concern very small and patchy regions and will thus not be analysed further.

As indicated above, the significant PPP in the subpolar North Atlantic Ocean is robust across the four ensembles. The PPP of the annual SST integrated over the Atlantic subpolar region (40–70°N) remains high during the first 10 years of forecast range (not shown) in all ensembles, and this is also the case for the SST averaged over the whole North Atlantic (Fig. 2d). The high predictability in the North Atlantic is suggested to be related to the Atlantic meridional overturning circulation (AMOC) in many studies (e.g. Msadek et al. 2010) and more specifically in our model (Persechino et al. 2013; Mignot et al. 2015). In accordance with these studies, the AMOC exhibits significant predictability up to 10 years ahead for all ensembles, and even up to 20 years in ATM (Fig. 2f). The temperature averaged in the intermediate and deep ocean (300 m to the bottom, T300) exhibits significant predictability over a timescale of at least 20 year (Fig. 2h). However, the PPP in ATM is not found to be significantly different from the PPP in oceanic perturbed ensembles, neither on the AMOC nor on SST or T300 average. No clear impact can be found either in terms of ensemble mean according to a t test of the 95 % level except for few randomly distributed lags, likely due to the insufficient number of members for robust statistics. This confirms the lack of clear impact of the perturbation strategy on the predictability assessment.

Several conclusions can be drawn from these results. Firstly, oceanic uncertainties as simulated by a white noise perturbation of the temperature field do not lead to higher spread of oceanic indices than atmospheric perturbations only. This does not depend on the tested amplitudes of the perturbation, since 3D, 3D10 and 3D100 (not shown) lead to similar quantitative result. Secondly, on interannual to decadal timescales, the deep ocean anomalies perturb the system as efficiently as the full ocean or the atmosphere. This contradicts the idea that the slow and weakly variable deep ocean should only lead to a slow and weak divergence of the ensemble. To understand the similarities of the four ensembles behaviour, the following section describes the error growth due to the initial perturbation into the system at short time scales (from daily to monthly).

4 Error growth analysis

4.1 Surface

To investigate the rapid response of the atmosphere and oceanic surface to each perturbation, we consider the daily evolution of the error growth of sea level pressure (SLP), SST and oceanic temperature at 100 m depth (T100). Because daily values could be saved for one member only for each ensemble, the commonly used ensemble spread is not available and we thus consider the daily evolution of the Euclidean distance (hereafter norm) between the perturbed (one DEC member) and the unperturbed (CTL) variable fields (Fig. 3). This can be mathematically written as:

$$\varepsilon(t) = \sqrt{\frac{1}{S_{tot}} \int_{S_{tot}} (X_{DEC}(t) - X_{CTL}(t))^2 dS}, \qquad (2)$$

where S_{tot} is the total surface of the global ocean, dS is the unit surface, and X_{DEC} and X_{CTL} are the considered variable (e.g. SLP, SST or T100) in one member of any DEC ensemble and in CTL, respectively. The so-defined norm $\varepsilon(t)$ gives an assessment of the error between the perturbed and unperturbed (CTL) simulations. The upper expected limit of this norm is $\sqrt{2}$ times the norm of the daily standard deviation field of the de-seasonalized variable X in CTL. The $\sqrt{2}$ factor is explained by the variance of a difference between two time series being the sum of variance of each time series. As each time series ($X_{DEC}(t)$ and $X_{CTL}(t)$) have the same variance in our case, it implies a factor of two.

Figure 3 shows the time evolution of this norm during the first 3 months for the SLP (a), and during the
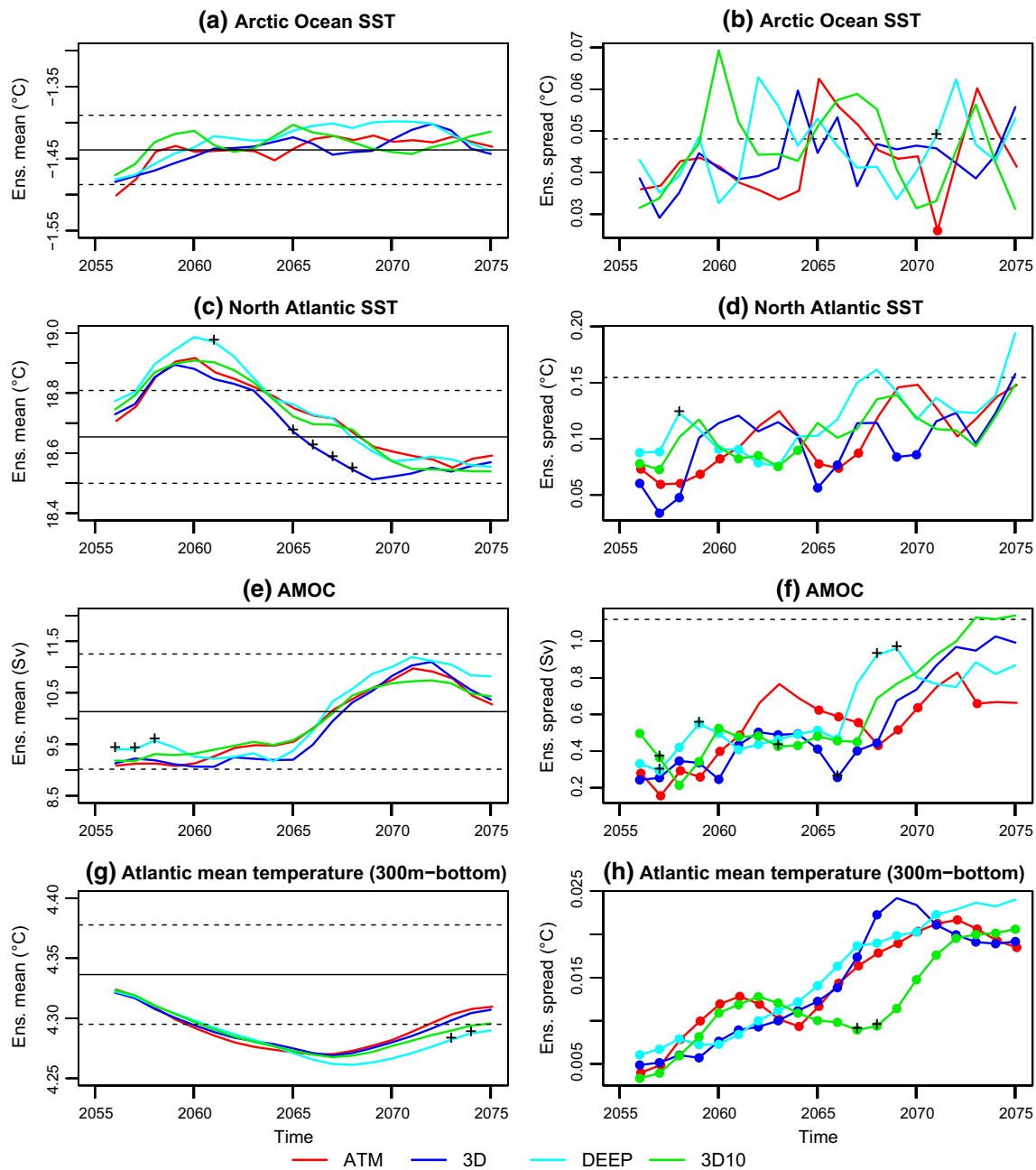
Fig. 2 **a**, **c**, **e**, **g** Ensemble mean of the SST averaged over the Arctic Ocean delimited by the Bering strait, the Fram strait, and the Barent sea opening (*1st row*), the SST averaged over 0–60°N (*2nd row*), the AMOC defined as the maximum value of the zonal mean stream function in [0–60°N, 500–2000 m] (*3rd row*), and the North Atlantic mean temperature averaged over 300 m to the bottom (*4th row*), as a function of lead-time. *The black* and *dashed lines* correspond to the whole CTL time series (1000-year long) average and one STD interval respectively. **b**, **d**, **f**, **h** Ensemble spreads, computed as the ensemble STD from the ensemble mean, as a function of lead-time. *The black dashed line* corresponds to the STD of CTL. *Full circles* cor-

respond to values significantly different from the CTL STD according to a Fisher test at the 95-confidence level. The number of degrees of freedom of the ensemble spread estimation is taken as 9 considering each member as independent, while for CTL it is computed taking into account the autocorrelation of the time series (Bretherton et al. 1999). All indices are smoothed by a 3-year running mean before the ensemble mean and STD are computed. In **b**–**h** *black crosses* correspond to ensemble mean and spread significantly different from the one of ATM, according to a 95-confidence level Student and Fisher test respectively
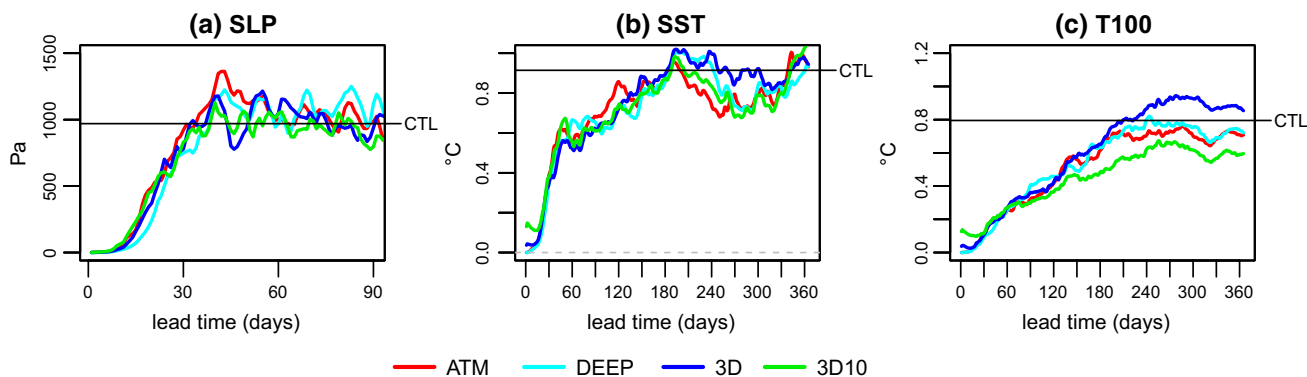
first year for the SST (b), and T100 (c). The SLP error growth (Fig. 3a) increases very slowly during approximately the first 10 days. A clear break is then noticeable

from which it increases rapidly until approximately day 30, after which it saturates. The strong increase in the error between the perturbed simulations and the control

Fig. 3 Daily time series of the Euclidean distance between the perturbed (one DEC ensemble member) and unperturbed (CTL) simulations for the SLP (**a**), SST (**b**), and T100 (**c**). The SST is taken as the ocean temperature in the first depth level, which is 10 m thick. *The black thin line* corresponds to the natural variability of the tempera-ture anomalies, assessed as $\sqrt{2}$ times the Euclidean norm of the CTL daily STD field once the seasonal cycle removed. Note that the $\sqrt{2}$ factor is explained by the variance of the difference between two time series of the same variance being twice the variance of the time series
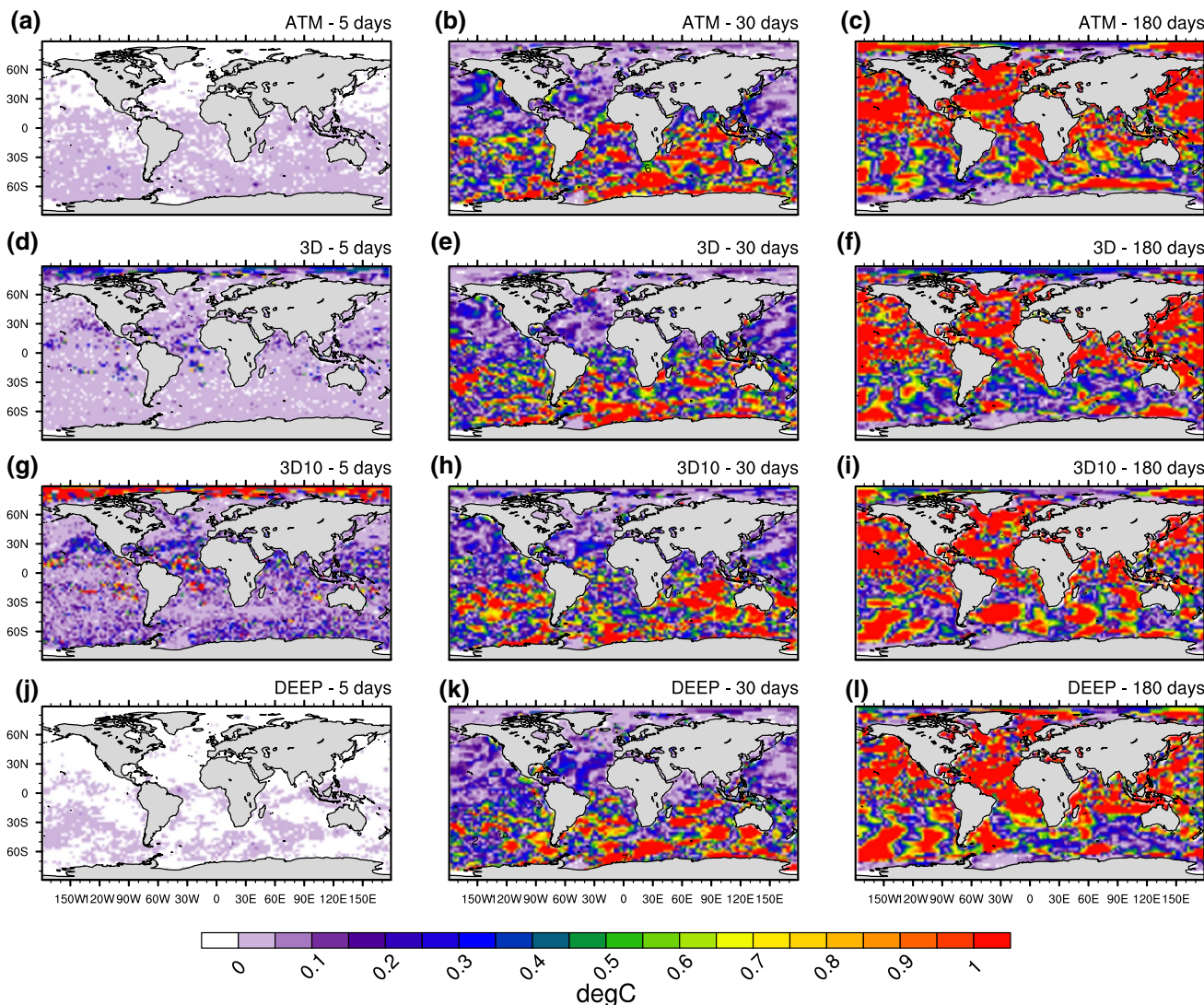

Fig. 4 ATM (*1st row*), 3D (*2nd row*), 3D10 (*3rd row*), and DEEP (*4th row*) SST anomaly field referring to CTL at 5 (*1st column*), 30 (*2nd column*) and 180 (*3rd column*) days forecast range. The SST anomaly field is normed by $\sqrt{2}$ times the CTL daily STD field once the seasonal cycle removed

after 10 days is consistent with the well-known weather predictability limit being around 2 weeks (Lorenz 1969; Buizza 2010). Similar timescale has also been found in an atmospheric model (J. Annan and W. Connolley, pers. com.). Interestingly, this error growth behaviour and this timescale are similar regardless of the initial perturbation strategy. It is even the case for DEEP, where the initial perturbation did not concern the surface of the ocean, and thus one would have expected a delayed impact on the atmosphere. Yet, even though the perturbation of the oceanic surface fields on very short timescale may be less intuitive in DEEP, it can be explained from simple dynamical considerations. For instance, consider a case with a temperature anomaly applied in only one grid cell (called C hereafter) at the bottom of the ocean. At the first time step, because of the pressure anomaly induced by the temperature anomaly, a dynamical adjustment leads to an anomalous horizontal current between cell C and the adjacent cells on the horizontal. Due to mass conservation under incompressible assumption in the model, the 3D divergence of the velocity field is null, so that a vertical anomalous velocity is generated in the entire water column above cell C and the adjacent cells. These vertical motions induce an anomalous vertical advection up to the surface where it creates (as in the rest of the water column) a temperature anomaly during the first numerical model time stepping and an impact on atmospheric surface fields after the first coupling time step (i.e. 1 day). This indicates that surface fields can be expected to be modified by the end of the first model day in all the ensembles, including DEEP. Figure 3b shows that on the first day of simulation, the SST norm is distributed as expected from the perturbation strategies of the oceanic initial state, that is $\varepsilon_{3D10} > \varepsilon_{3D} > \varepsilon_{DEEP}$. ε_{ATM} and ε_{DEEP} are initially very small (~3.6 × 10^{-5} °C), but different from zero as anticipated. As indicated in Sect. 2, note that there is no round off errors in the restart files of DEEP compared to the ones of CTL above 2000 m, meaning that this very small error is, indeed, coming from a response to the deep perturbation. This initial perturbation then transmits to the atmosphere.

At the weekly to monthly timescale, the SST error growth exhibits roughly the same feature as for the SLP, i.e. a slow increase followed by a very fast error growth toward the saturation value. However, unlike for the SLP, the SST fast error growth ends around day 60 while the saturation value is reached around day 180. In between, an additional regime with slower SST error growth can be identified, and
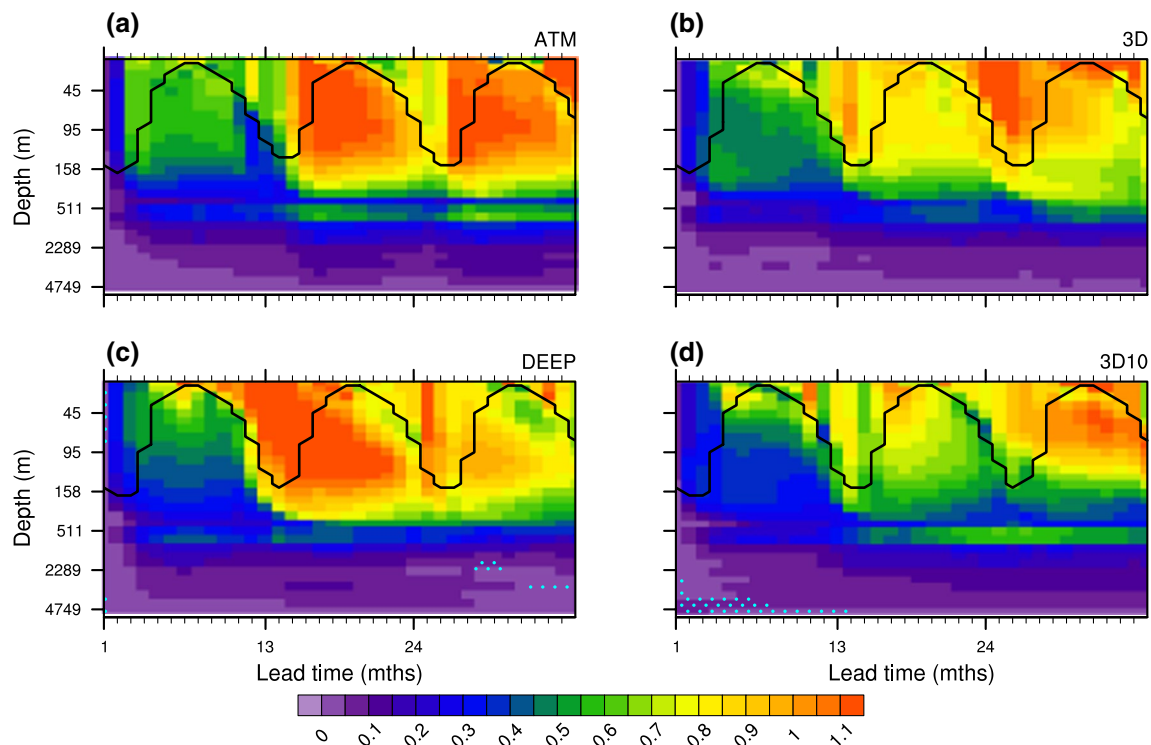

Fig. 5 Hovmöller diagram of the spatially averaged oceanic temperature ensemble spread as a function of depth and lead-time (in months). The temperature is horizontally averaged over the North Atlantic zonal band [30°N–40°N] at each depth. The ensemble spread is normalized by the STD in CTL for the corresponding climatological month and depth. *The black line* corresponds to the ensemble mean of the averaged mixed layer depth over the same domain. In **b–d**, the *cyan dots* highlights the areas where the ensemble spread is significantly different from the one of ATM according to a Fisher test at 95-confidence level

attributed to the integration effect of the ocean. This regime is more prominent at depth as the influence of the atmosphere decreases, as evidenced for T100 (Fig. 3c) which exhibits a slower error growth, indicative of an integration of the surface error growth.

As for the SLP, SST and T100, error growth does not depend on the ensemble generation strategy. Figure 4 illustrates the spatial distribution of the SST error growth during the three main regimes that are (1) the first low rate increase of the norm (day 5, 1st column), (2) the fast error growth regime (day 30, 2nd column), and (3) the error growth saturation (day 180, 3rd column). It confirms that

the spread of all ensembles exhibit similar behaviour also in terms of spatial distribution and the perturbation strategies cannot be distinguished from one another once the fast error growth has started.

To conclude, all perturbation strategies result in a rapid (less than a month) spread of the SST and SLP at the global scale. The fast error growth initiated by oceanic perturbation for 3D, 3D10 and DEEP, is mainly taken over by the atmospheric component. This error growth slows down in deeper layers where the daily time scale is less relevant. Thus, we now investigate the time evolution of the ensemble spread in the interior ocean at the monthly time scale.
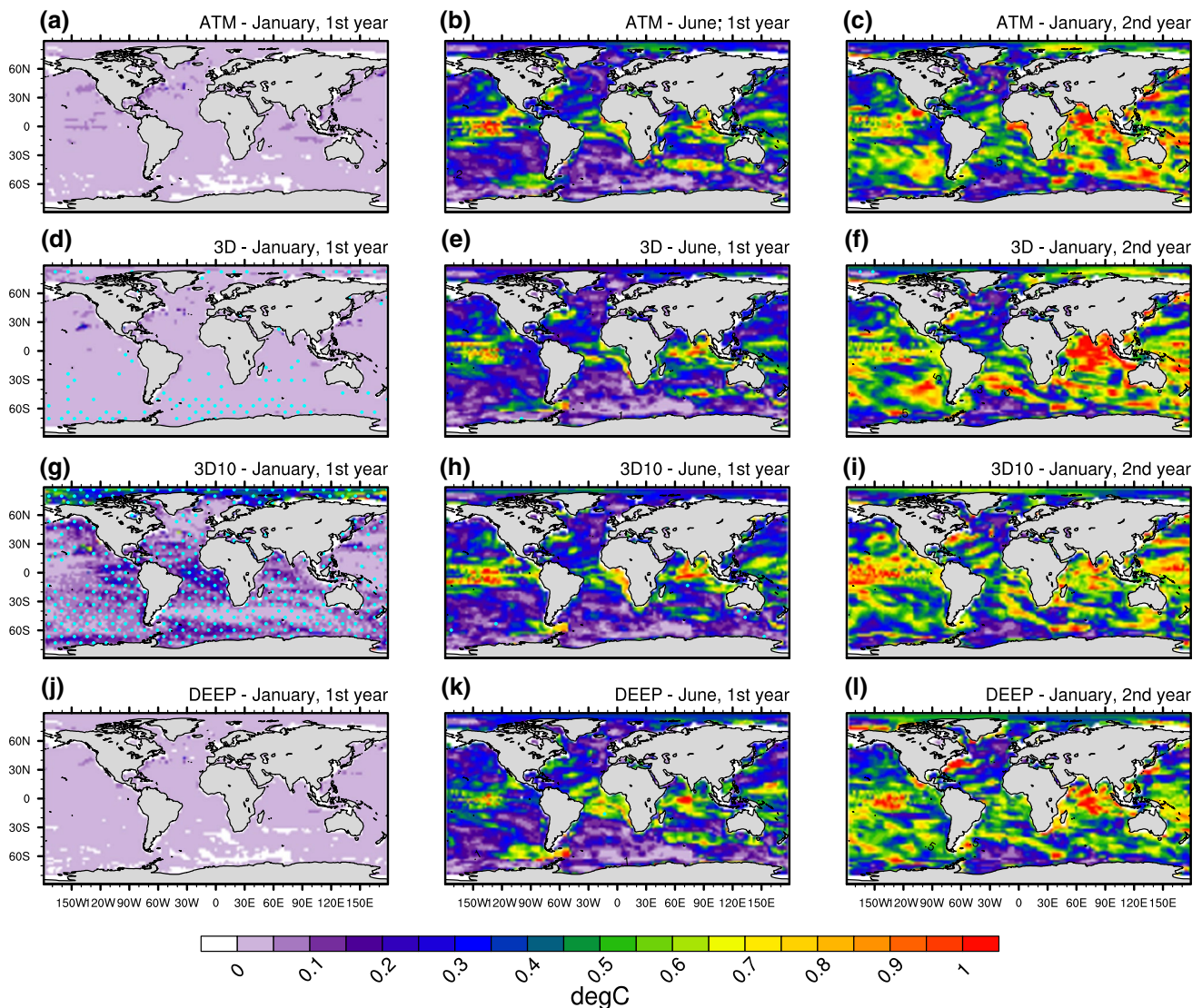

Fig. 6 ATM (*1st row*), 3D (*2nd row*), 3D10 (*3rd row*), and DEEP (*4th row*) ensemble spread of the oceanic temperature at 140 m depth at 1 (*1st column*), 6 (*2nd column*) and 13 (*3rd column*) months forecast range. The ensemble spread in normed by the STD of January (*1st* and *3rd columns*) and June (*2nd column*) interannual oceanic temperature field in CTL. In **a**, **d**, **g** and **j**, the *cyan dots* highlights the areas where the ensemble spread is significantly different from the one of ATM according to a Fisher test at 95-confidence level

4.2 Water column

In the aim of identifying which part of the water column exhibits the strongest divergence and how this divergence evolves, we look at the monthly ensemble spread of spatially averaged oceanic temperatures for each vertical level of the ocean model. In order to take into account the strong disparities of the temperature temporal variability at different depths, and thus expected disparities in the ensemble spread, the STD computed in CTL for the corresponding climatological month and vertical level normalizes the latter. Figure 5 shows a Hovmöller plot of this ratio averaged in the zonal band 30–40°N in the Atlantic for each ensemble. As for shorter timescales, all ensembles exhibit the same pattern of time-depth evolution for the monthly temperature spread. The spread ratio remains very weak in the deep ocean (below 800 m in the area shown in Fig. 5) during the whole 20-year long integrations, despite a slow increase (not visible in the figure). At the surface

and at intermediate depths, the spread growth is relatively fast, consistently with Fig. 3 and much stronger. It develops after the first 3 months, primarily at the surface, and a propagation pattern from the surface toward the ocean interior follows during the next fall/winter. This penetration pattern occurs in the four DEC ensembles without any strong differences due to the initial perturbation strategy. This cycle is repeated each fall/winter, and the penetration is associated with the winter Mixed Layer (ML) deepening (black lines in Fig. 5). Note that the ensemble spread of the ML depth itself is weak (not shown) indicating that the same depths are ventilated in each member. The fact that the ratio increases from the surface suggests that the spread comes initially from ocean–atmosphere interactions. Thus, we conclude that the temperature error growth at depth results from modified water mass characteristics in the mixed layer through air-sea interactions, which are then ventilated in the ocean interior. The 30–40°N zonal band in the Atlantic corresponds to the subtropical mode water
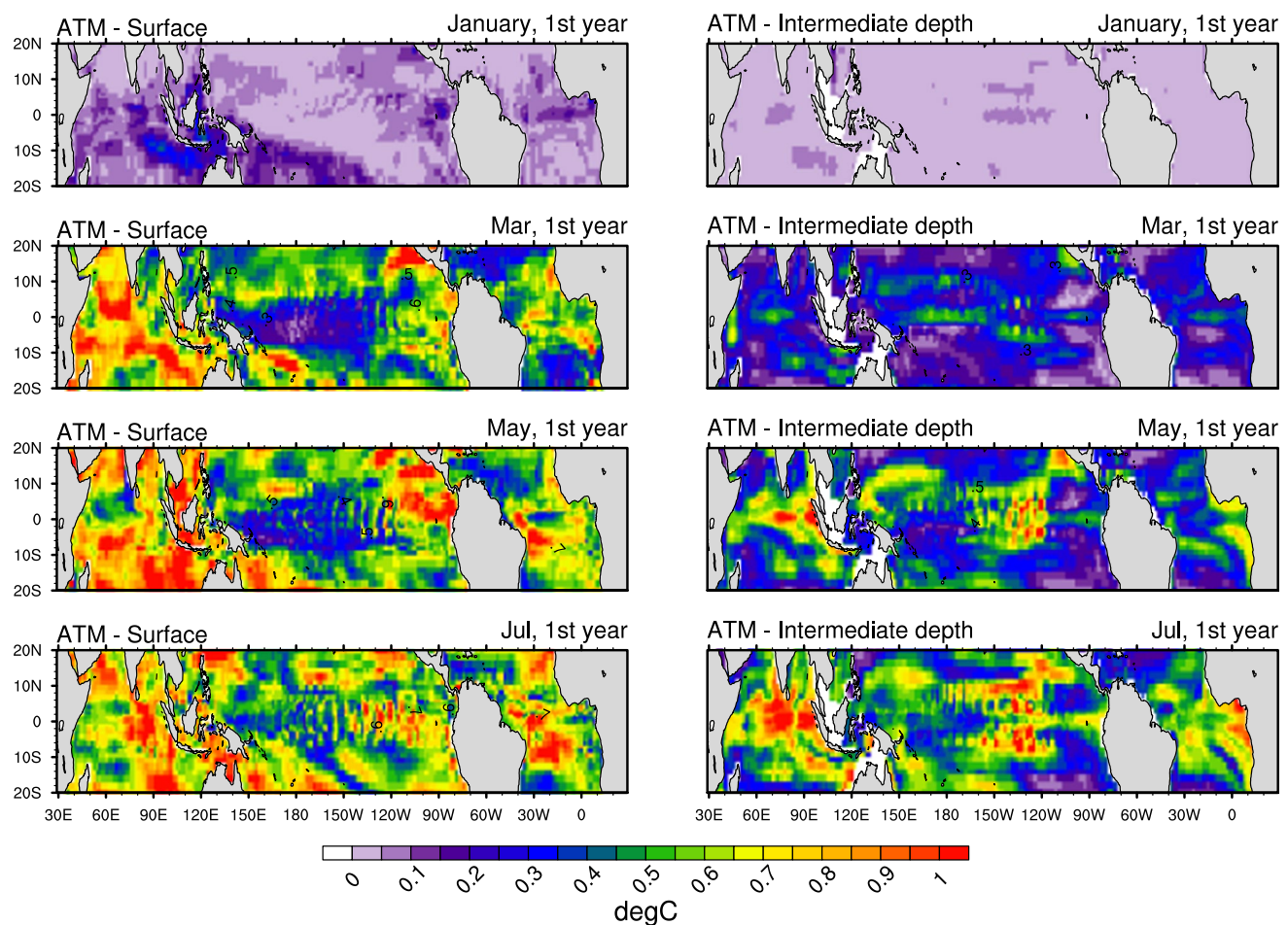

Fig. 7 ATM ensemble spread of the oceanic temperature at the surface (*1st column*) and 140 m depth (*2nd column*) for the first January (*1st row*), March (*2nd row*), May (*3rd row*), and July (*4th row*). The ensemble spread in normed by the STD of January (*1st and 3rd columns*) and June (*2nd column*) interannual oceanic temperature field in CTL (same as in Fig. 6)
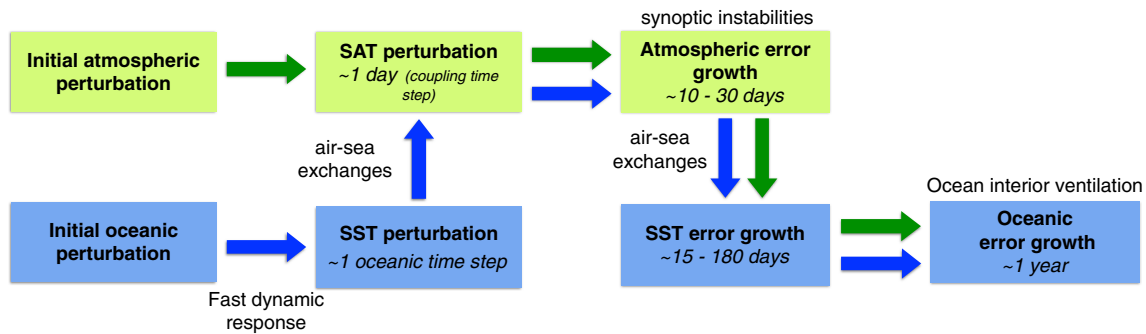
Fig. 8 Schematic representation of the processes leading to dominant oceanic error growth identified in this analysis (*large green* and *blue arrows*), and the associated time scales. This process, mainly driven by the atmospheric chaotic behaviour, might co-exist with an internal subduction where, after the seasonal ventilation, the newly formed water masses are capped by the seasonal thermocline, and can be advected away from the formation area (e.g. Hanawa and Talley 2001; Kolodziejczyk et al. 2015), leading to divergence among ensemble members in the ocean interior possibly affecting surrounding latitudinal bands after the first year.

Except for the equatorial band, similar penetration pattern can be identified in every zonal band of the North Pacific and North Atlantic oceans (not shown), yet with a propagation depth and time depending on the latitude. This depth corresponds to the ML maximum seasonal deepening. In the equatorial band, no vertical propagation pattern can be identified in accordance with the very weak ML seasonal cycle there. Figure 6 shows the spatial distribution of the error growth computed as in Fig. 5 at 140 m depth and three different time steps for the four ensembles. This depth has been chosen as it is sensible to the seasonal ventilation in the mid latitudes and crosses the thermocline in the equatorial Pacific. This figure highlights the contrast between tropical and mid-latitudes regions, the spread growing faster in the first ones as compared to the second ones during the first year, whatever the initial perturbation strategy is (Fig. 6, 2nd column). At mid-latitudes, the spatial structure emphasizes the rapid divergence in areas of strong temperature and salinity horizontal front, such as western boundary currents and the Antarctic circumpolar current in the South Hemisphere (Fig. 6, 2nd and 3rd column). In the tropical areas, it rather exhibits a zonal pattern, with fastest error growth along the equator and around 10°N and 10°S. This structure is especially clear in the central Pacific Ocean and suggests that the error growth comes from Kelvin (equatorial band) and Rossby (10°N and 10°S) waves propagation (Philander et al. 1984). It grows rapidly and can be clearly identified after only 2 months as shown in Fig. 7 (2nd column) for ATM. In contrast to extratropical regions, at these locations, the spread remains weaker at the surface (Fig. 7, 1st column). This contrast between the surface and the subsurface further suggests a wave adjustment, which move preferably along the subsurface thermocline. Furthermore, the zonal contrast in the subsurface Pacific Ocean reflects the zonal slope of the thermocline, the larger spread being found where the thermocline crosses the 140 m isodepth (in the centre of the basin in the IPSL-CM5A-LR model, not shown).

The oceanic perturbed ensembles (i.e. 3D, 3D10 and DEEP) exhibits no significant difference compared to ATM except for the first month (Fig. 6, 1st column) where the differences still reflect the different initial perturbation strategies. Therefore, atmospheric only perturbations are sufficient to trigger this error growth. This is in accordance with the observed rapid adjustment of the thermocline coming from wind anomalies (Johnson and McPhaden 1993; Kessler et al. 1995). Then, the perturbation along the thermocline propagates following Kelvin and Rossby waves adjustment.

To summarize, the ensemble spread of the oceanic component is mainly driven by the atmosphere, with two distinct mechanisms propagating the signal into the upper ocean interior: while the seasonal ML deepening dominates in the mid and high latitudes, thermocline adjustment to wind anomalies dominates in the tropics.

5 Discussion and conclusions

Four ensembles generated with perturbations in their initial state at different locations, mimicking observational uncertainties, have been performed and analysed. We found that regardless of the location of initial perturbation—atmosphere, ocean, or the deep ocean—it results in triggering the atmospheric error growth through the SST field within the first day. The atmospheric component error growth reaches its saturation value after roughly 1 month

of forecast. This atmospheric error growth, in turn, impacts SST through air-sea exchanges, which explain the SST error growth patterns that we have found in our different perturbed ensembles. Finally, in the mid and high latitudes, ventilation processes integrate the signal from the surface ocean to the interior, following the seasonal deepening of the mixed layer, on the time scale of a year. In the tropics, the ocean thermocline responds rapidly to perturbed wind forcing anomalies, producing out-of-phase Kelvin and Rossby waves that increase the ensemble spread in the thermocline. The error growth of the oceanic component is thus dominated by its response to the perturbed atmosphere. This is schematically summarized in Fig. 8. The high sensitivity of the atmosphere to the initial disturbances, and its dominant role in the initial error growth, results in a similar evolution of the system despite a different initial perturbation strategy. This explains the similar behaviour of the ensembles regarding interannual climate index evolution. One limitation of this study is that these results might depend on the chosen start date. Yet, according to Persechino et al. (2013), our start date exhibits a moderate AMOC predictive skill compared to the average of other different start dates. This suggests that, although some predictors have been identified regarding this peculiar start date, it is unlikely that these predictors strongly reduced the sensitivity to initial perturbations.

This analysis shows that oceanic uncertainties as represented by a white noise on the oceanic temperature field have no additional impact on the interannual behaviour of the ensemble, and therefore on the predictability assessment, than an atmospheric-only perturbation. Nevertheless the mesoscale oceanic dynamics might play an important role in oceanic instability growth by dramatically increasing the ocean sensitivity to initial conditions disturbances. Our results thus need to be confirmed with an eddy resolving oceanic component model. However, decadal experiments being very expensive in terms of computing resources, the moderate oceanic resolution of our model is not uncommon in near-term climate prediction analyses. Therefore, our analysis gives useful insight on the impact of oceanic initial perturbations in state-of-the-art decadal experiments.

The euclidian norm of the white noise initial perturbation field used in this study goes from 0.005 °C for 3D to 0.05 °C for 3D10. These values are comparable to the norm of the perturbation field obtained by classical 1- and 5-day lag perturbation, which are around 0.01 and 0.03 °C respectively (based on 1- and 5-day lag temperature field anomaly computed in CTL over the start date year, i.e. 2056). However, despite these comparable values of the global anomaly field norm, the pattern of the perturbation differs strongly between the two methods. Indeed, the day

lag perturbation field exhibits some large-scale anomalies typical of ocean dynamical features, such as waves and shifts of oceanic fronts (not shown). Taking into account our knowledge of the ocean dynamic and ocean uncertainties (i.e. the imperfect accuracy of the initial state in addition to imperfect precision) would indeed imply to use spatial pattern of the perturbation differing from the white noise. Du et al. (2012) showed that oceanic perturbations obtained from using different oceanic reanalyses tend to increase the spread of oceanic variables in comparison to atmospheric-only perturbations. In their set up, the pattern of initial perturbation anomalies most likely account for typical variability patterns of the ocean dynamics, the accuracy, as well as the precision of the initial state estimation. In Romanova and Hense (2015), the anomaly pattern account for ocean dynamics at a chosen time scale. As for the daily lag method and the use of different oceanic reanalyses, this procedure gives more importance to large-scale anomalies than small-scale ones, which is more likely to perturb the geostrophic balance of the large-scale circulation. On the contrary, the white noise used here gives the same importance to all scales by construction. Thus small-scale errors, which can be rapidly damped by mixing in the ocean, may be artificially overestimated at the expense of large-scale perturbations, which are likely to persist and thus to efficiently perturb the climatically-relevant large-scale ocean dynamics. This difference of spatial frequencies might play a key role in the oceanic response in terms of spread. Further analyses are needed to characterize how the scale of initial perturbation affects the intensity of the spread of the oceanic component. More generally, we need to understand why, when, and how the direct oceanic error growth will be efficient enough to induce a larger oceanic error growth than the ocean–atmosphere error growth mechanism identified in our study. In this aim, the use of oceanic optimal error growth perturbations as described in Sévellec and Fedorov (2013) is a promising perspective.

References

Abraham JP, Baringer M, Bindoff NL, Boyer T, Cheng LJ, Church JA, Conroy JL, Dominguez CM, Fasullo JT, Gilson J, Goni G, Good SA, Gorman JM, Gouretski V, Ishii M, Johnson GC, Kizu S, Lyman JM, Macdonald AM, Minkowycz WJ, Moffitt SE, Palmer MD, Piola AR, Reseghetti F, Schuckmann K, Trenberth KE, Velicogna I, Willis JK (2013) A review of global ocean temperature observations: implications for ocean heat content estimates and climate change. Rev Geophys 51(3):450–483. doi:10.1002/rog.20022

Aumont O, Bopp L (2006) Globalizing results from ocean in situ iron fertilization studies. Glob Biogeochem Cycles 20, GB2017. doi:10.1029/2005GB002591

Baehr J, Piontek R (2014) Ensemble initialization of the oceanic component of a coupled model through bred vectors at seasonal-to-interannual timescales. Geosci Model Dev 7(1):453–461. doi:10.5194/gmd-7-453-2014

Bellucci A, Gualdi S, Masina S, Storto A, Scoccimarro E, Cagnazzo C, Fogli P, Manzini E, Navarra A (2013) Decadal climate predictions with a coupled OAGCM initialized with oceanic reanalyses. Clim Dyn 40(5–6):1483–1497. doi:10.1007/s00382-012-1468-z

Born A, Mignot J, Stocker T (2015) Multiple equilibria as a possible mechanism for decadal variability in the North Atlantic Ocean. J Clim 28:8907–8922

Branstator G, and Teng H (2010) Two limits of initial-value decadal predictability in a CGCM. Journal of climate 23(23):6292–6311. doi:10.1175/2010JCLI3678.1

Bretherton CS, Widmann M, Dymniko VP, Wallace JM, Bladé I (1999) The effective number of spatial degrees of freedom of a time-varying field. J Clim 12:1990–2009

Buchan J, Hirschi JJM, Blaker AT, Sinha B (2014) North Atlantic SST anomalies and the cold North European weather events of winter 2009/10 and December 2010. Mon Weather Rev 142(2):922–932. doi:10.1175/MWR-D-13-00104.1

Buizza R (2010) Horizontal resolution impact on short-and long-range forecast error. Q J R Meteorol Soc 136(649):1020–1035. doi:10.1002/qj.613

Collins M, Botzet M, Carril AF, Drange H, Jouzeau A, Latif M, Masina S, Otteraa AH, Pohlmann H, Sorteberg A, Sutton R, Terray L (2006) Interannual to decadal climate predictability in the North Atlantic: a multimodel-ensemble study. J Clim 19(7):1195–1203. doi:10.1175/JCLI3654.1

Du H, Doblas-Reyes FJ, García-Serrano J, Guemas V, Soufflet Y, Wouters B (2012) Sensitivity of decadal predictions to the initial atmospheric and oceanic perturbations. Clim Dyn 39(7–8):2013–2023. doi:10.1007/s00382-011-1285-9

Dufresne JL, Foujols M-A, Denvil M-AS, Caubel A, Marti O, Aumont O, Balkanski Y, Bekki S, Bellenger H, Benshila R, Bony S, Bopp L, Braconnot P, Brockmann P, Cadule P, Cheruy F, Codron F, Cozic A, Cugnet D, de Noblet N, Duval J-P, Ethé C, Fairhead L, Fichefet T, Flavoni S, Friedlingstein P, Grandpeix J-Y, Guez L, Guilyardi E, Hauglustaine D, Hourdin F, Idelkadi A, Ghattas J, Joussaume S, Kageyama M, Krinner G, Labetoulle S, Lahellec A, Lefebvre M-P, Lefevre F, Levy C, Li ZX, Lloyd J, Lott F, Madec G, Mancip M, Marchand M, Masson S, Meurdesoif Y, Mignot J, Musat I, Parouty S, Polcher J, Rio C, Schulz M, Swingedouw D, Szopa S, Talandier C, Terray P, Viovy N, Vuichard N (2013) Climate change projections using the IPSL-CM5 Earth System Model: from CMIP3 to CMIP5. Clim Dyn 40(9–10):2123–2165. doi:10.1007/s00382-012-1636-1

Fichefet T, Maqueda MAM (1997) Sensitivity of a global sea ice model to the treatment of ice thermodynamics and dynamics. J Geophys Res 102:2609–2612

Goldenberg SB, Landsea CW, Mestas-Nuñez AM, Gray WM (2001) The recent increase in Atlantic hurricane activity: causes and implications. Science 293(5529):474–479. doi:10.1126/science.1060040

Griffies SM, Bryan K (1997) A predictability study of simulated North Atlantic multidecadal variability. Clim Dyn 13(7–8):459–487. doi:10.1007/s003820050177

Ham YG, Rienecker MM, Suarez MJ, Vikhliaev Y, Zhao B, Marshak J, Verniere G, Schubert SD (2014) Decadal prediction skill in the GEOS-5 forecast system. Clim Dyn. doi:10.1007/s00382-013-1858-x

Hanawa K, Talley LD (2001) Mode waters. Int Geophys Ser 77:373–386

Hazeleger W, Wouters B, Oldenborgh GJ, Corti S, Palmer T, Smith D, Storch JS (2013) Predicting multiyear north atlantic ocean variability. J Geophys Res 118(3):1087–1098. doi:10.1002/jgrc.20117

Hourdin F, Foujols M-A, Codron F (2013) Impact of the LMDZ atmospheric grid configuration on the climate and sensitivity of the IPSL-CM5A coupled model. Clim Dyn. doi:10.1007/s00382-012-1411-3

Johnson E, McPhaden MJ (1993) Structure of intraseasonal Kelvin waves in the equatorial Pacific Ocean. J Phys Oceanogr 23:608–625. doi:10.1175/1520-0485(1993)023<0608:SOIKWI>2.0.CO;2

Karspeck AR, Stammer D, Köhl A, Danabasoglu G, Balmaseda M, Smith DM, Fujii Y, Zhang S, Giese B, Tsujino H, Rosati A (2015) Comparison of the Atlantic meridional overturning circulation between 1960 and 2007 in six ocean reanalysis products. Clim Dyn. doi:10.1007/s00382-015-2787-7

Keenlyside NS, Latif M, Jungclaus J, Kornblueh L, Roeckner E (2008) Advancing decadal-scale climate prediction in the North Atlantic sector. Nature 453(7191):84–88

Kennedy JJ (2014) A review of uncertainty in in situ measurements and data sets of sea surface temperature. Rev Geophys 52(1):1–32. doi:10.1002/2013RG000434

Kessler WS, McPhaden JM, Weickmann KM (1995) Forcing of intraseasonal Kelvin waves in the equatorial Pacific. J Geophys Res 100(C6):10–613

Kirtman B, Power SB, Adedoyin JA, Boer GJ, Bojariu R, Camilloni I, Doblas-Reyes FJ, Fiore AM, Kimoto M, Meehl GA, Prather M, Sarr A, Schär C, Sutton R, van Oldenborgh GJ, Vecchi G, Wang HJ (2013) Near-term climate change: projections and predictability. In: Stocker TF, Qin D, Plattner G-K, Tignor M, Allen SK, Boschung J, Nauels A, Xia Y, Bex V, Midgley PM (eds) Climate change 2013: the physical science basis. Contribution of working group I to the fifth assessment report of the intergovernmental panel on climate change. Cambridge University Press, Cambridge

Kolodziejczyk N, Reverdin G, Lazar A (2015) Interannual variability of the mixed layer winter convection and spice injection in the eastern subtropical North Atlantic. J Phys Oceanogr 45(2):504–525

Kröger J, Müller WA, Von Storch JS (2012) Impact of different ocean reanalyses on decadal climate prediction. Clim Dyn 39:795–810. doi:10.1007/s00382-012-1310-7

Lorenz EN (1963) Deterministic nonperiodic flow. J Atmos Sci 20(2):130–141

Lorenz EN (1969) Atmospheric predictability as revealed by naturally occurring analogues. J Atmos Sci 26(4):636–646

Madec G (2008) NEMO ocean engine, Technical note, IPSL. Available at http://www.nemo-ocean.eu/content/download/11245/56055/file/NEMO_book_v3_2.pdf

McCarthy GD, Haigh ID, Hirschi JJM, Grist JP, Smeed DA (2015) Ocean impact on decadal Atlantic climate variability revealed by sea-level observations. Nature 521(7553):508–510. doi:10.1038/nature14491

Mignot J, Swingedouw D, Deshayes J, Marti O, Talandier C, Séférian R, Lengaigne M, Madec G (2013) On the evolution of the oceanic component of the IPSL climate models from CMIP3 to CMIP5: a mean state comparison. Ocean Model 72:167–184. doi:10.1016/j.ocemod.2013.09.001

Mignot J, Garcia-Serrano J, Swingedouw D, Germe A, Nguyen S, Ortega P, Guilyardi E, Ray S (2015) Decadal prediction skill in the ocean with surface nudging in the IPSL-CM5A-LR climate model. Clim Dyn. doi:10.1007/s00382-015-2898-1

Msadek R, Dixon KW, Delworth TL, Hurlin W (2010) Assessing the predictability of the Atlantic meridional overturning circulation and associated fingerprints. Geophys Res Lett. doi:10.1029/2010GL044517

Müller WA, Pohlmann H, Sienz F, Smith D (2014) Decadal climate predictions for the period 1901–2010 with a coupled climate model. Geophys Res Lett 41(6):2100–2107. doi:10.1002/2014GL059259

Ortega P, Mignot J, Swingedouw D, Sévellec F, Guilyardi E (2015) Reconciling two alternative mechanisms behind bi-decadal variability in the North Atlantic. Prog Oceanogr 137:237–249. doi:10.1016/j.pocean.2015.06.009

Peings Y, Magnusdottir G (2014) Forcing of the wintertime atmospheric circulation by the multidecadal fluctuations of the North Atlantic ocean. Environ Res Lett 9(3):034018. doi:10.1088/1748-9326/9/3/034018

Persechino A, Mignot J, Swingedouw D, Labetoulle S, Guilyardi E (2013) Decadal predictability of the Atlantic meridional overturning circulation and climate in the IPSL-CM5A-LR model. Clim Dyn 40(9–10):2359–2380. doi:10.1007/s00382-012-1466-1

Philander SGH, Yamagata T, Pacanowski RC (1984) Unstable air–sea interactions in the tropics. J Atmos Sci 41:604–613. doi:10.1175/1520-0469(1984)041<0604:UASIIT>2.0.CO;2

Pohlmann H, Botzet M, Latif M, Roesch A, Wild M, Tschuck P (2004) Estimating the decadal predictability of a coupled AOGCM. J Clim 17(22):4463–4472. doi:10.1175/3209.1

Pohlmann H, Smith DM, Balmaseda MA, Keenlyside NS, Masina S, Matei D, Müller WA, Rogel P (2013) Predictability of the mid-latitude Atlantic meridional overturning circulation in a multi-model system. Clim Dyn 41(3–4):775–785. doi:10.1007/s00382-013-1663-6

Ray S, Swingedouw D, Mignot J, Guilyardi E (2014) Effect of surface restoring on subsurface variability in a climate model during 1949–2005. Clim Dyn. doi:10.1007/s00382-014-2358-3

Romanova V, Hense A (2015) Anomaly transform methods based on total energy and ocean heat content norms for generating ocean dynamic disturbances for ensemble climate forecasts. Clim Dyn. doi:10.1007/s00382-015-2567-4

Sanchez-Gomez E, Cassou C, Ruprich-Robert Y, Fernandez E, Terray L (2015) Drift dynamics in a coupled model initialized for decadal forecasts. Clim Dyn. doi:10.1007/s00382-015-2678-y

Séférian R, Bopp L, Gehlen M, Orr JC, Ethé C, Cadule P, Aumont O, Salas y Mélia D, Voldoire A, Madec G (2013) Skill assessment of three earth system models with common marine biogeochemistry. Clim Dyn 40(9–10):2549–2573. doi:10.1007/s00382-012-1362-8

Servonnat J, Mignot J, Guilyardi E, Swingedouw D, Séférian R, Labetoulle S (2014) Reconstructing the subsurface ocean decadal variability, using surface nudging in a perfect model framework. Clim Dyn. doi:10.1007/s00382-014-2184-7

Sévellec F, Fedorov AV (2013) Model bias reduction and the limits of oceanic decadal predictability: importance of the deep ocean. J Clim 26(11):3688–3707. doi:10.1175/JCLI-D-12-00199.1

Smith DM, Cusack S, Colman AW, Folland CK, Harris GR, Murphy JM (2007) Improved surface temperature prediction for the coming decade from a global climate model. Science 317(5839):796–799. doi:10.1126/science.1139540

Stan C, Kirtman BP (2008) The influence of atmospheric noise and uncertainty in ocean initial conditions on the limit of predictability in a coupled GCM. J Clim 21(14):3487–3503. doi:10.1175/2007JCLI2071.1

Stockdale TN, Anderson DLT, Alves JOS, Balmaseda MA (1998) Global seasonal rainfall forecasts using a coupled ocean–atmosphere model. Nature 392(6674):370–373. doi:10.1038/32861

Sutton RW, Dong B (2012) Atlantic Ocean influence on a shift in European climate in the 1990s. Nat Geosci. doi:10.1038/ngeo1595

Sutton RT, Hodson DL (2005) Atlantic Ocean forcing of North American and European summer climate. Science 309(5731):115–118. doi:10.1126/science.1109496

Swingedouw D, Mignot J, Labetoulle S, Guilyardi E, Madec G (2013) Initialisation and predictability of the AMOC over the last 50 years in a climate model. Clim Dyn 40(9–10):2381–2399. doi:10.1007/s00382-012-1516-8

Valcke S (2006) OASIS3 user guide (prism_2-5), technical report TR/CMGC/06/73, PRISM report no 2. CERFACS, Toulouse, p 60

Zhang R, Delworth TL (2006) Impact of Atlantic multidecadal oscillations on India/Sahel rainfall and Atlantic hurricanes. Geophys Res Lett. doi:10.1029/2006GL026267